

# An Adaptive Integration Time CMOS Image Sensor With Multiple Readout Channels

Xinyuan Qian, Hang Yu, Shoushun Chen, *Member, IEEE*, and Kay Soon Low, *Senior Member, IEEE*

**Abstract**—In this paper, we present an adaptive integration time CMOS image sensor with multiple readout channels for star tracker application. The sensor architecture allows each pixel to have an adaptive integration time. Through cyclically selecting a row of pixels and checking the integration voltage of each pixel, brighter pixels can be marked and readout first. Those dimmer pixels will continue integration until their voltage fall into a window defined by two threshold voltages. Each pixel only consists of five transistors. To improve the readout throughput and hence to reduce the rolling time, a multiple readout channel architecture is proposed. A proof-of-concept  $320 \times 128$ -pixel image sensor was implemented using Global Foundries  $0.18 \mu\text{m}$  mixed-signal CMOS process.

**Index Terms**—CMOS image sensor, adaptive integration time, multiple readout channels, high dynamic range (HDR), wide dynamic range (WDR), star tracker.

## I. INTRODUCTION

RECENT years have witnessed a trend in space technology that highlights the importance of mini and micro satellite missions. Earth-observation satellites need automatic attitude control system to steer the satellite to the desired observation point. Therefore many satellites are equipped with various navigation sensors (Earth magnetic, gyros, Sun sensor and star tracker) and observation sensors (imaging camera). Among these sensors, star trackers are the most accurate solution with a bore sight accuracy in the range of arcseconds [1].

Star radiation is measured by its visual magnitude. A star with Apparent Magnitude  $M_V=1$  is 2.5 times brighter than a magnitude  $M_V=2$  star. Using the Sun as reference, which has an Apparent Magnitude of  $M_V=-26.76$  and solar flux of  $1.3 \text{ KW/m}^2$ , we can easily derive any other star's luminance [2]. By taking into factors such as luminance spectral distribution, photo detector's quantum efficiency (QE) and lens point spread function (PSF), we can estimate the number of generated photons received by the camera. For a star tracker with 3 cm lens aperture, 85% lens transmission

efficiency, 1 pixel PSF, and 200 ms exposure time, a  $M_V=6$  star can generate 1195 photons at the center pixel of the star. In order to achieve higher altitude accuracy, it is preferable to shorten the exposure time. In the above calculation, 200 ms already produces a systematic error of 48 arc-second for an orbital period of 90 minutes. With a shorter exposure time, say 50 ms, the number of photons at the center pixel of a  $M_V=6$  star will drop to only 298. This is a very challenging number for CMOS image sensor, and in particular, under space radiation environment. A typical star tracker camera has a sensitivity to capture visual magnitude  $M_V < 5$ .

Recently, various solutions for high dynamic range (DR) CMOS image sensors have been proposed. Some of them take advantage of improved pixel architecture, whereas others use novel readout methods. In general, they can be categorized into four main methods [3], namely: logarithmic response [4]–[6], well capacity adjustment [7]–[9], multiple sampling [10], [11] and saturation detection [12]–[14]. In particular, the scheme of “saturation detection” allows each pixel to have adaptive integration time by detecting the time to reach the saturation state. The light intensity is then represented by the time domain (PWM) encoding [15] or frequency domain (PFM) encoding [16]. At the pixel level, it incorporates comparison and memory circuits, which results in complicated silicon implementation and hence large pixel footprint. This makes it difficult for high-resolution applications.

We propose a new architecture for the CMOS image sensor in which each pixel features an adaptive integration time. The adaptive integration time is achieved by cyclically checking the integration voltage of pixels in a row-wise manner during the exposure. In this case, brighter pixels can be “marked” and read out first. In order to improve the readout throughput, a scheme of multiple readout channel is proposed.

The rest of the paper is organized as follows. Section II introduces the architecture, operation principle and circuit design. Section III discusses the implementation and measurements results. Section IV draws a conclusion.

## II. OPERATION PRINCIPLE

The proposed architecture features column-parallel comparison circuits to decide whether a pixel should stop its integration or not. Fig. 1 illustrates the operation principle with an example of a  $3 \times 3$  pixel array. Initially, the sensor is globally reset and all the pixels start integration. Immediately followed by the reset operation, a row-wise scanner starts rolling. At  $T_0$ , *Row0* is selected and all the pixels in *Row0* are simultaneously sampled onto the column-parallel comparison circuits. In this example and at this moment, no pixel has

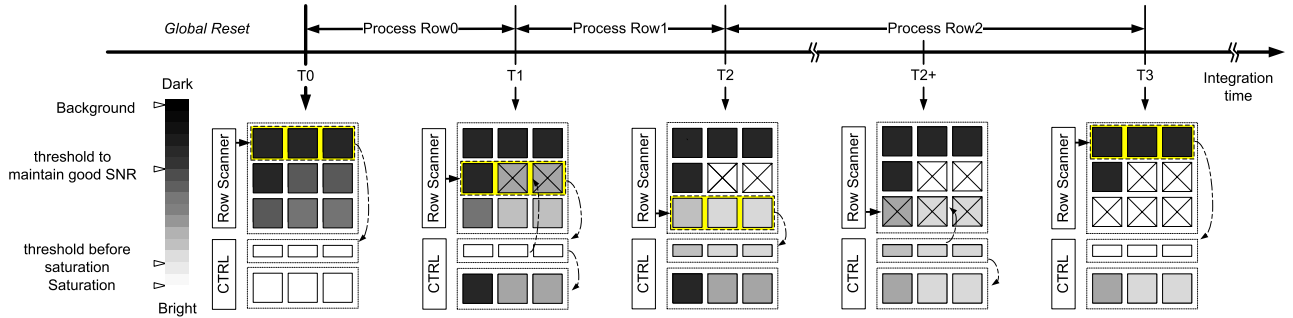


Fig. 1. Operation principle of the adaptive-integration-time readout scheme.

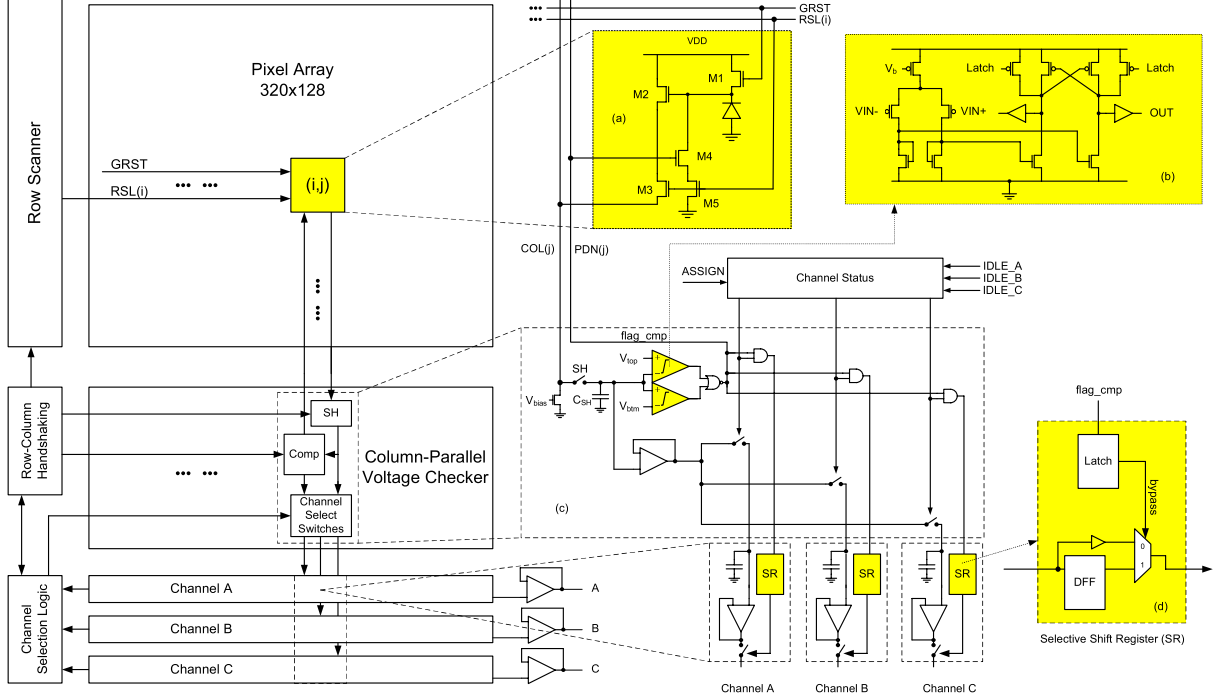


Fig. 2. Sensor architecture. Main building blocks include a pixel array, column-parallel comparison circuits, three readout channels, row scanner and channel assignment controller.

gathered enough photons and therefore none of the pixel's voltage falls into the threshold window. Next at time  $T1$ ,  $Row1$  is sampled and checked in the same manner. There are two bright pixels ( $Col1$ ,  $Col2$ ) and their voltage is within the threshold. This will enable the readout process and the whole  $Row1$  is assigned to a readout channel. In the meanwhile, the column circuits will raise a flag signal to “mark-off” the two bright pixels. In this way, these two pixels will be ignored in the future checking process. The readout channel takes two clock cycles to readout the active pixels in  $Row1$ . Instead of waiting for the completion of readout, the sensor continues to check  $Row2$  immediately after channel assignment. A pipeline mechanism has been proposed so that the voltage checking and readout can work in parallel. In the case that all readout channels are occupied, at time  $T3$  for example, the row-wise scanner will pause until at least one channel is free. For a particular row, the readout time is proportional to the number of “active” pixels. This is implemented by a scanner with bypass control. When the row scanner hits the last row, it will loop back to the first row to scan another round.

### III. SENSOR ARCHITECTURE

The architecture of the proposed image sensor is shown in Fig. 2. It includes a  $320 \times 128$  pixel array, column-parallel comparison circuits, multiple(three) readout channels, a row scanner, a channel assignment controller and a global timer. The pixel array is globally reset by  $GRST$ . As can be seen from Fig. 2(a), each pixel consists of five nMOS transistors.  $M1 - M3$  forms a typical Active Pixel Sensor (APS). Two extra transistors  $M4 - M5$  form a pull-down path for the photodiode. As such, the photodiode can be pulled down to its saturation level by external control signal. The column-parallel comparison circuits reside at the bottom of the pixel array and communicate with the pixel through two vertical buses,  $COL(j)$  and  $PDN(j)$ . The column-parallel comparison circuits is composed of a SH circuit block, comparison circuits and a group of channel select switches. The comparator, as shown in Fig. 2(b), is a static-latched type with pre-amplifier stage [17], [18]. The regeneration node is decoupled by two current mirrors for low kickback noise. In each readout channel, the

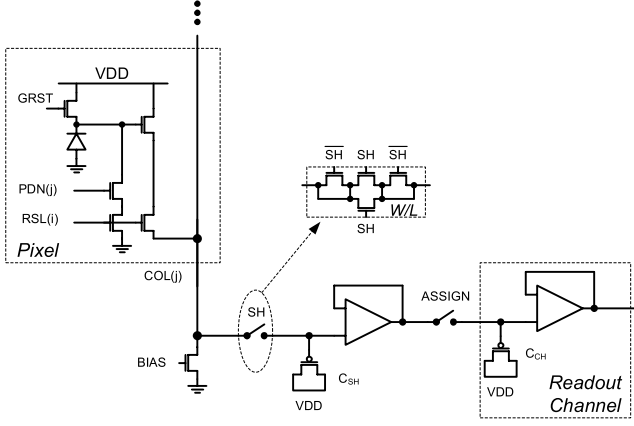


Fig. 3. Analog signal path from the pixel to a readout channel.

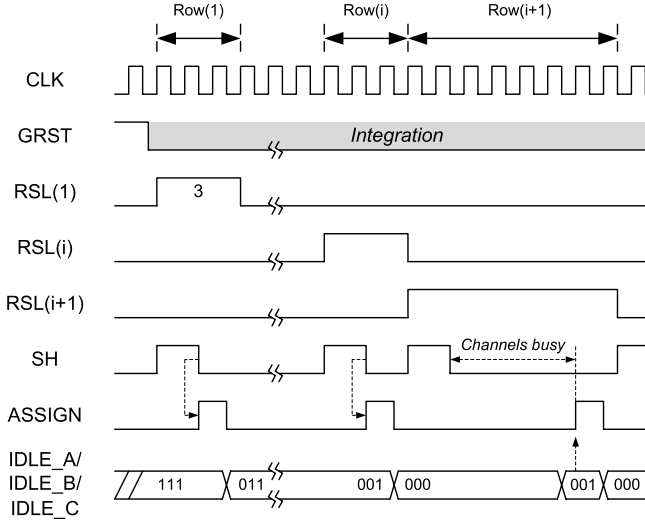


Fig. 4. Timing diagram of the sensor operation.

scan register can be configured to bypass a certain column depending on the comparison result. The channel selection logic allows to decide which channel can be used to read out a selected row.

#### A. Analog Path

Fig. 3 highlights the analog path from the pixel to the readout channel and Fig. 4 shows the corresponding timing diagram of the sensor operation, respectively. Two stages of sample-and-hold circuits are required for the pixel voltage to transfer to the analog global buffer. During the cycles when row select signal  $RSL(i)$  is  $ON$ , the pixel voltage is first sampled-and-held onto  $C_{SH}$  within one and half cycles. In order to minimize the sampling error caused by the critical channel charge injection, the single SH transistor switch is replaced by four identical nMOS transistors to suppress the charge injection onto  $C_{SH}$ . Followed by the SH operation, ASSIGN switch will be turned on to transfer the pixel voltage on  $C_{SH}$  to the corresponding local sample-and-hold capacitor  $C_{CH}$  in the channel once a channel becomes “IDLE”. The design of ASSIGN switch is the same of the SH switch to minimize the effect of channel charge injection. The analog

buffer to drive the next stage is a seven-transistor two-stage operational amplifier. Since the pixel voltage after the source follower stays at the lower range of the power supply, both  $C_{SH}$  and  $C_{CH}$  are designed to be pMOS capacitors. Consideration has also been taken to design the size of both capacitors. As in the scenarios when  $RSL(i+1)$  is  $ON$ , all channels are busy after SH, the sampled pixel voltage on  $C_{SH}$  must hold until it is allowed to transfer to  $C_{CH}$ . Due to the leakage current across the capacitor, this long delay can cause the voltage on  $C_{SH}$  to drop from its expected value. The worst-case delay is approximately 320 clock cycles when all channels are just occupied by other rows. For  $C_{CH}$  in the readout channel, on the other hand, the worst case to withstand the leakage current is the one in the last column, which must hold the voltage until all previous columns are readout. This also amounts approximately to 320 clock cycles. Both  $C_{SH}$  and  $C_{CH}$  are designed to be  $6\mu\text{m} \times 2.8\mu\text{m}$  large and approximately 135fF according to the simulation results. This limits the voltage drop due to leakage current on the capacitor as low as within 0.5LSB after 32us at 10MHz clock frequency.

#### B. Readout Channel Assignment

The sampled pixel voltage on capacitor  $C_{SH}$  is compared to two threshold voltages namely  $V_{top}$  and  $V_{bottom}$ , respectively. The comparison result is fed back to the array and the pixel is “marked-off” by pulling down the diode voltage using transistor  $M4$ . At the same time, the result is stored in a latch and further used as a bypass control for the column-wise scanner. The shift register at a specific column is therefore skipped when  $flag_{cmp} = 0$  and hence a row with less “active” pixels will take shorter readout time.

Our architecture builds three readout channels, which are managed by a channel selection logic. Each channel has a flag register indicating the status of “BUSY” or “IDLE”. The assignment logic uses a simple priority rule to manage the three channels. Channel A has the highest priority and Channel C will be used only when both Channel A and B are unavailable. Once a channel is identified as “IDLE”, the assignment switches will be turned on and the analog voltage will be transferred from capacitor  $C_{SH}$  to the corresponding local sample-and-hold capacitor in the channel.

#### C. Image Reconstruction

With this scheme, pixels with different illumination level will have their own integration time. The principle is further illustrated in Fig. 5. *PixelA* experiences a sharper discharge slope due to a larger photocurrent. *PixelB* shows a moderate photocurrent while *PixelC* is apparently under dark condition. We can set a maximum allowable integration time and those pixels (*PixelC*, for example) that fail to reach the readout window will be considered as dark pixels. The sensor outputs both analog voltage and the time stamp when the voltage is sampled. Both the time ( $t_s$ ) and voltage ( $V_s$ ) information are used to reconstruct the picture:

$$I_{ph} = \frac{C_{int} \cdot (V_{rst} - V_s)}{t_s} \quad (1)$$

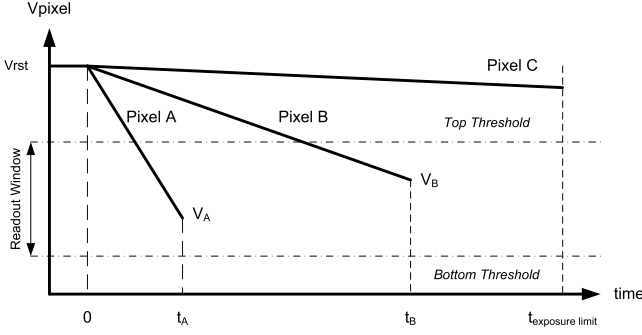


Fig. 5. Illustration of different pixel's response. Pixels with different illumination level will have its own integration time.

where  $I_{ph}$  is the pixel's photocurrent and  $C_{int}$  is the photodiode capacitance.

#### D. Dynamic Range

Dynamic range of the sensor architecture is given by the following expression:

$$DR = 20 \log \frac{I_{max}}{I_{min}} = 20 \log \frac{C_{int} (V_{rst} - V_{btm}) / t_{min}}{C_{int} (V_{rst} - V_{top}) / t_{max}} \quad (2)$$

where  $I_{max}$  and  $I_{min}$  are the maximum and minimum photocurrents that can be detected in the pixel, respectively.  $C_{int}$  is the photodiode capacitance,  $V_{rst}$  is the pixel reset voltage,  $V_{btm}$  is the bottom threshold and  $V_{top}$  is the top threshold, respectively.  $t_{max}$  is the longest integration time, which is the exposure time limit.  $t_{min}$  is the shortest integration time, which is integration time for a certain pixel in the first-round voltage checking.  $t_{min}$  can be regarded as the waiting time for a pixel to be processed due to row-wise scanning. The minimum of this waiting time is one and half cycles for the first row of pixels since their voltages are checked immediately after reset.

If the sensor operates at 10MHz, that is, 100ns per clock cycle,  $t_{min}$  is then 150ns.  $t_{max}$  is assumed to be 300ms. Also given that  $V_{rst}$ ,  $V_{top}$  and  $V_{btm}$  are set to 1V, 0.8V and 0.2V, respectively, DR of 138dB is expected.

## IV. SIMULATION RESULTS

In order to simulate the sensor architecture proposed in this paper, we developed a MATLAB-based simulator. The MATLAB program simulates the operation principle including photo-detection, row-wise scanning, column-wise comparison readout channel assignment with corresponding timing. A 12-bit (ranging 0-4095) grayscale image with  $320 \times 128$  pixels is first translated into a photocurrent array in terms of digital numbers (DN). The photocurrent array is used as the input of the simulator. For column-parallel voltage comparison, both top threshold and bottom threshold that form the readout window are user variables so that one can evaluate this design parameter as will be explained later. According to the proposed sensor operation, there are three readout channels used in simulation. The pixel values across the array are updated in each cycle. The timing of comparison operation is set to two cycles and the assignment lasts for one cycle before the row scanner switches to the next row. Throughout

the integration, those pixels that have been readout are marked as one while zero for those that miss the readout. The reconstructed image is obtained by multiplying the marked results with the original image. Therefore, those pixels that miss the readout become "black" pixels in the final output.

Fig. 6 shows the simulation results of a Lena image. In the first group, as shown in (a)-(d), top threshold is set to 3500 and bottom thresholds are 1500, 2500, 3000 and 3300, respectively. Second group, (e)-(h), configures the top threshold to 3000 and bottom thresholds are 1000, 2000, 2500, 2800, respectively. Last group, (i)-(l), configures top threshold to 2500 and bottom thresholds are 500, 1000, 2000 and 2300, respectively. Each group thus forms a readout window of 2000, 1000, 500 and 200, respectively. As can be seen from the comparison, one can clearly observe the "black" pixels exist increasingly across the pixel array with the shrinkage of the readout window. These "black" pixels not only exist in the dark region of the original image, but also occupy a large portion of the bright regions. These bright regions across the pixel array are likely to have similar photocurrent magnitude. Therefore if a large portion of these pixels require to be processed, it requires a large amount of time to finish before it proceeds to another region. During this time, other bright regions are still integrating and their pixel values are likely to fall below the readout window and therefore regarded as "black" pixels. Generally, the bottom threshold is set slightly above the saturation level to maximize the readout window. When comparing between groups with the same readout window size and different top threshold, one can find that these "black" regions generally shift. Top threshold determines the time for a pixel to fall into the readout window. The higher the top threshold, the earlier the pixel will trigger the readout process. The actual readout sequence is accordingly changed as well.

In general, the readout window should be set as wide as possible to increase the number of readouts. But the readout of a scene is still limited by a number of other parameters, for example, actual photocurrent size, pixel array size and readout bandwidth. As discussed earlier, if there are large regions with similar illumination level in the array, it can cause pixels in other regions to saturate before they can be handled. One can imagine of the worst-case of a uniform photocurrent array, where a complete row will be processed before it switches to the next. It will occupy the readout channel for long so as to cause other rows to saturate. On the other hand, if the imaging scene has a sparse distribution of similar illumination levels, for example, a star field, one can take advantages of this dynamic readout scheme.

Fig. 7 shows the simulation results of a star field image with the same parameter settings as the previous example. Stars are the regions of interest and has a sparse distribution of similar illumination levels. Although, some very bright stars saturate when the readout window is small, but they are all captured when the readout window becomes wide. And also due to wide distribution of the dark background in such a star field scene, most of the missing readouts are composed of these pixels, which is not of primary concern. Fig. 8(a) and (b) show the readout percentage of the Lena image and star image, respectively. Due to the

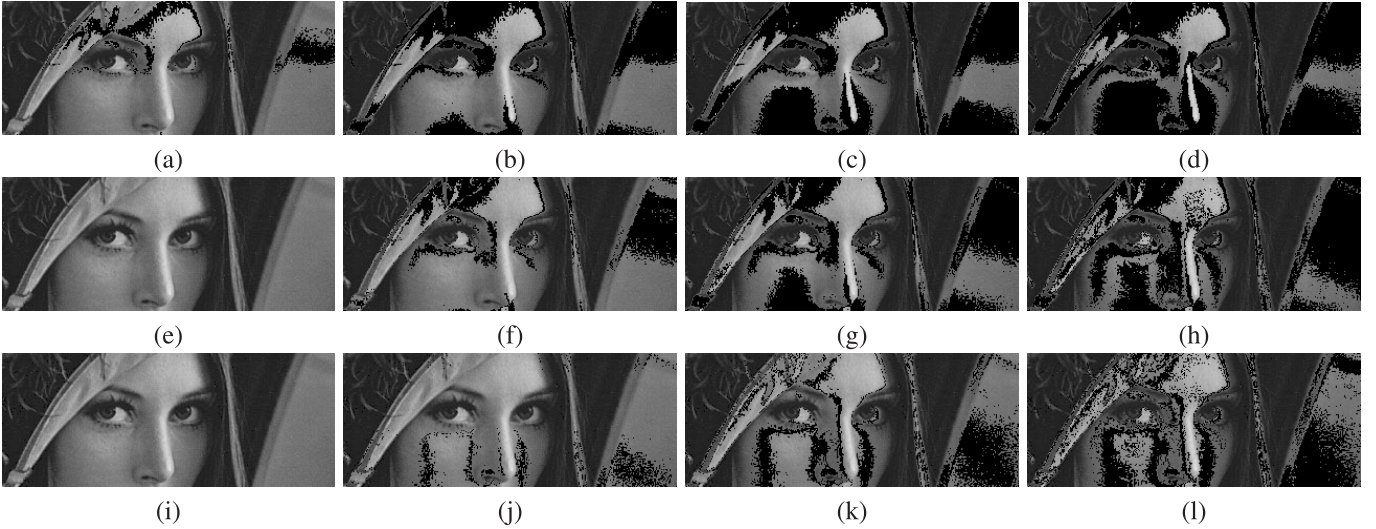


Fig. 6. Simulation results for a  $320 \times 128$  Lena image under sensor operation. In (a)-(d), top threshold is set to 3500 and bottom threshold are 1500, 2500, 3000 and 3300, respectively. In (e)-(h), top threshold is set to 3000 and bottom threshold are 1000, 2000, 2500, 2800, respectively. In (i)-(l), top threshold is set to 2500 and bottom threshold are 500, 1000, 2000 and 2300, respectively.

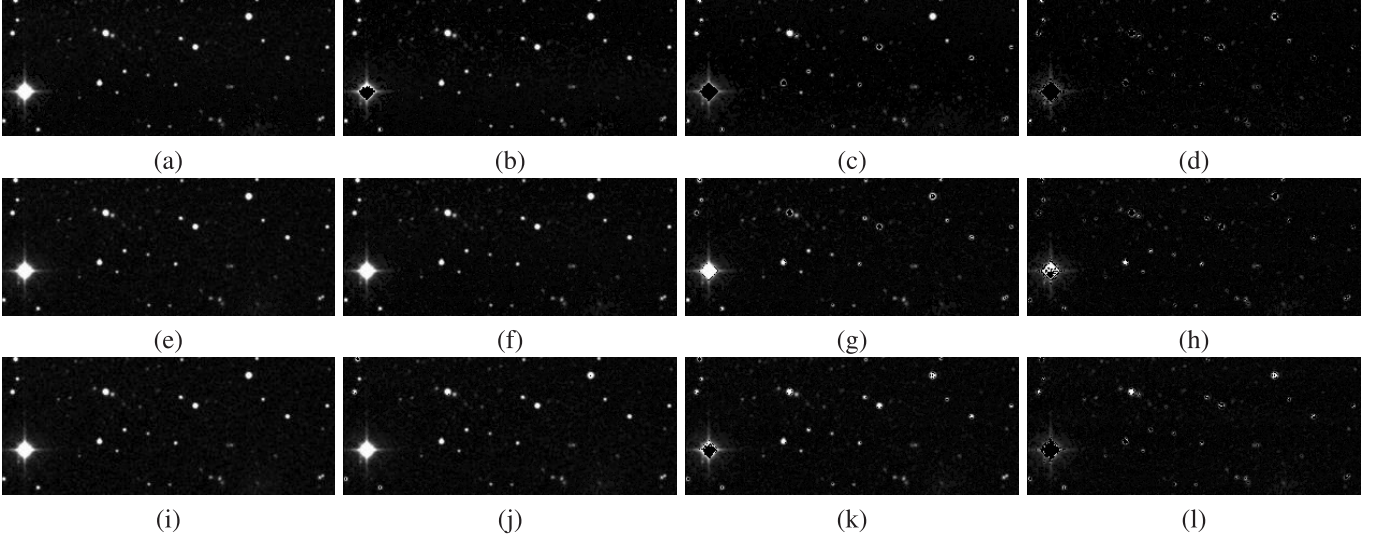


Fig. 7. Simulation results for a  $320 \times 128$  star field image under sensor operation. In (a)-(d), top threshold is set to 3500 and bottom threshold are 1500, 2500, 3000 and 3300, respectively. In (e)-(h), top threshold is set to 3000 and bottom threshold are 1000, 2000, 2500, 2800, respectively. In (i)-(l), top threshold is set to 2500 and bottom threshold are 500, 1000, 2000 and 2300, respectively.

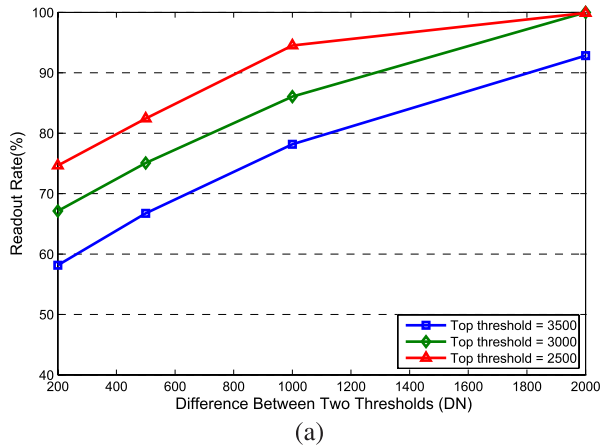
wide distribution of dark background, the overall statistic readout percentage of a star image (below 92%) happens to be smaller than that of Lena's for the same parameter settings. Nonetheless, from the image reconstruction, the stars are completely captured in all simulated scenarios.

## V. IMPLEMENTATION AND MEASUREMENT RESULTS

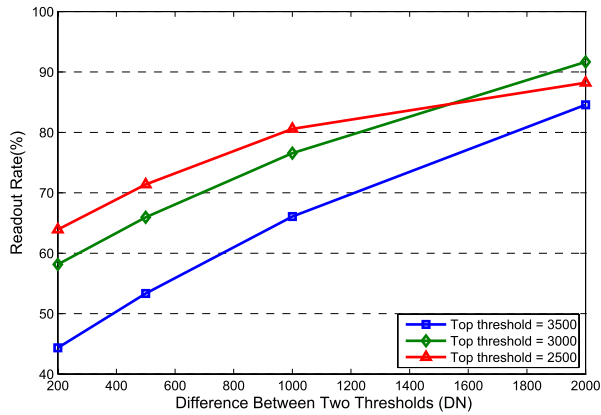
The proposed image sensor has been fabricated in Global Foundries  $0.18\mu\text{m}$  1P6M CMOS technology. Fig. 9 shows the chip microphotograph where the main building blocks are highlighted. The overall chip dimension is  $2.5 \times 2.5 \text{ mm}^2$ . The array contains  $320 \times 128$  pixels. Each pixel features a footprint of  $5 \times 5 \mu\text{m}^2$  with a fill-factor of 38%. The column-wise comparators with programmable threshold voltages are placed at the bottom of the pixel array. The chip has three readout channels. Each channel outputs signal pairs consisting

analog signal, time and column address. The row address is generated off-chip due to the sequential nature of the row scanner.

The sensor was interfaced with an Opal-Kelly XEM 3010 FPGA board. The FPGA acquires the output signals for each channel and temporarily store them on the on-board RAM. In addition, the FPGA also provide input control signals and communicate with a host PC through a USB link. The post-processing of the captured data and image reconstruction is conducted on PC. During sensor characterization, we have observed that the chosen process shows poor light response within the tested range up to 18klux. The average dark current is measured at  $1537\text{fA}$  for a N+/P-sub photodiode with an area of  $4.26\mu\text{m} \times 2.28\mu\text{m}$ . The sensor has a readout speed of 10MHz and consumes 247mW power. The sensor parameters and characterization details are listed in Table I.



(a)



(b)

Fig. 8. Readout percentage of the (a) Lena and (b) star image.

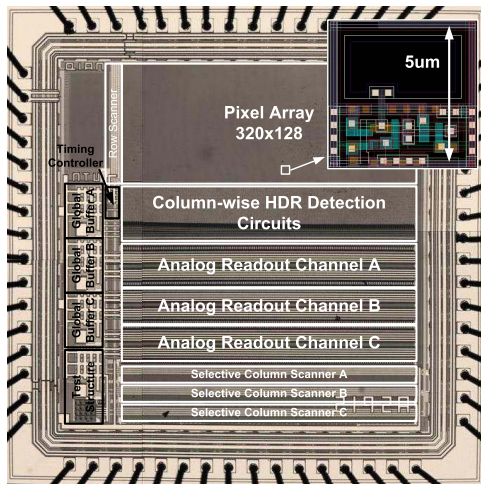


Fig. 9. Chip microphotograph.

Fig. 10 shows the relation between the incident light intensity and reconstructed photocurrent. The incident illumination varies from 0.1lux to approximately 200klux, which is uniformly exposed to the pixel array. The voltage of the pixel is firstly measured and photocurrent is then extrapolated using Eq. 1. The plotted results have offset the dark current. When the illumination approaches about 200klux, the pixel in the first row starts to saturate after 150ns integration. The total DR is therefore about 126dB.

TABLE I  
PERFORMANCE SUMMARY OF THE SENSOR

Technology	Global Foundry 0.18 $\mu$ m mixed-signal CMOS
Die Dimensions	2.5mm $\times$ 2.5mm
Supply Voltage	1.8V
Clock Frequency	10MHz
Power Consumption	247mW
Pixel Array Size	320(H) $\times$ 128(V)
Photodetector Type	N+/P-sub photodiode
Pixel size	5 $\mu$ m $\times$ 5 $\mu$ m
Fill Factor	38%
Signal Swing	180mV - 950mV
Temporal Noise	148e-
Sensitivity	0.25V/lux·s
FPN	1.6%

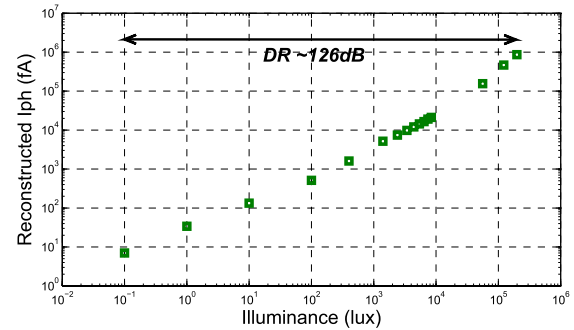


Fig. 10. Measured photocurrent with regard to incident illuminance.

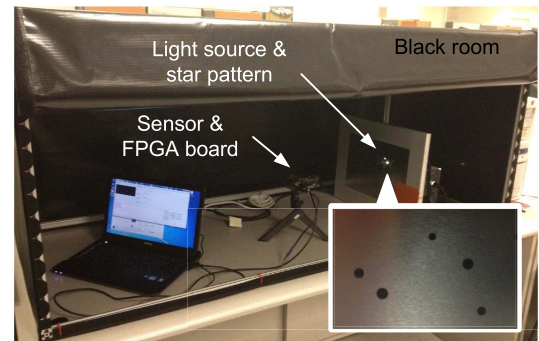


Fig. 11. Measurement setup for capturing "star" images.

#### A. Simulated Star-Pattern Measurement

The sensor is used to image the scene of star field where the star objects ("bright pixels") in the scene are of primary concern. In order to simulate the star field imaging, we have built a test platform as shown in Fig. 11. The star field is simulated by letting uniform light source back-illuminate through a star pattern mask. The star pattern is made of a PCB stencil with precise position control of the "stars". The light source generates approximately 10klux photons to pass through the star pattern and camera aperture. The measurement was done in a dark room. The sample images for simulated star-pattern measurement is shown in Fig. 12 under various parameter settings. We have swept the bottom threshold from

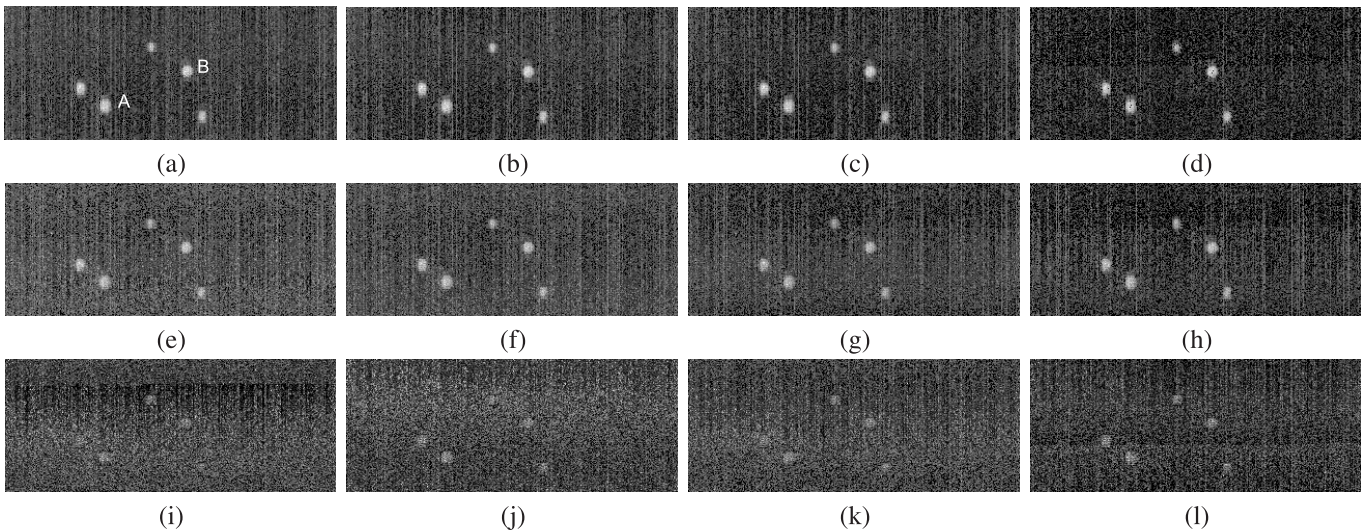


Fig. 12. Raw sample images for simulated star-pattern measurement under different parameter settings. Images in the first row (a)-(d), top threshold is set to 500mV and bottom threshold are 250mV, 300mV, 350mV and 450mV, respectively. In (e)-(h), top threshold is changed to 600mV and In (i)-(l), top threshold is set to 700mV. Two “stars”, marked as A and B, are selected for centroiding evaluation.

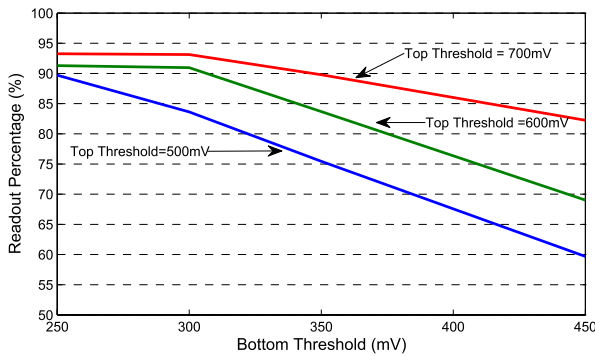


Fig. 13. Readout percentage of the simulated star-pattern images.

250mV to 450mV for three different top thresholds, respectively. The analog outputs of the sensor are converted to digital values by external Analog-to-Digital Converter (ADC). The photocurrent of each pixel is extrapolated using Eq. 1. Those unread pixels are regarded as dark pixels. To represent the image on the monitor, the obtained photocurrent data are further normalized to 8-bit gray-scale pixel values. The sample images are raw star image without any post processing and compensation.

As discussed earlier in our simulation results, both top threshold and bottom threshold play an important role in readout pixel numbers. Fig. 13 shows the corresponding readout percentage with different size of the readout window. It is clear that the readout percentage drops with the shrinking of the readout window. Most of the missing readouts are located in the dark background. The diversely-distributed “stars”, objects in interest, are completely captured except when the readout window decreases down to 50mV, as shown in Fig. 13(c). Missing readouts start to appear inside “stars”, which leads to measurement errors in star intensity.

The star illumination in a star sensor is used to calculate the star location. Utilizing its intensity values on a mass of pixels, the location of the “star” can be represented by

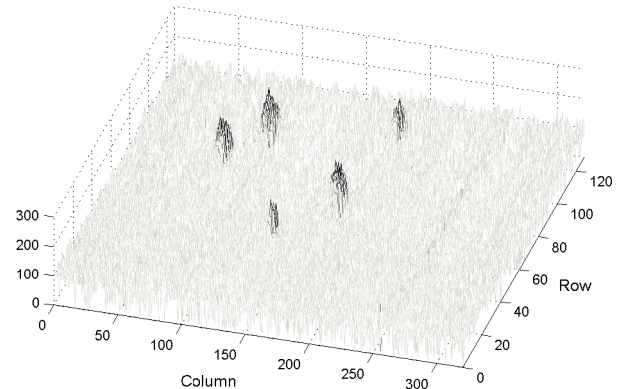


Fig. 14. Gray-scale mapping of the star image in Fig. 12(a).

its centroid position. We implement star centroiding [2] to assess the measurement accuracy. Fig. 14 shows the gray-scale illumination mapping of the sample star image after image reconstruction. All of the stars are captured without pixel saturation. The relative distances between the “stars” are used as the benchmark to evaluate the precision. Two “stars” and their distance are selected for evaluation as shown in Fig. 12(a). The ideal coordinates of “star” A(63, 97) and “star” B(96, 176) are used. The relative distance between the “stars” is 85.62 pixels (33 pixels horizontally and 49 pixels vertically) in the star pattern stencil. The calculated distance errors for all tested scenarios are illustrated in Fig. 15. We have observed sub-pixel errors for most of the tested scenarios. Top threshold has shown significant effect on the calculation error compared with bottom threshold. The absolute calculated error is above 0.89 pixels when the top threshold is 700mV. The increase in the top threshold will cause the readout of “star” pixels to be triggered earlier with small signal magnitude. It implies that for these “star” pixels, a decreased number of the photons are received during readout. The centroiding accuracy has strong dependence on the number of the received photons [2]. In addition, the position error is also contributed by several

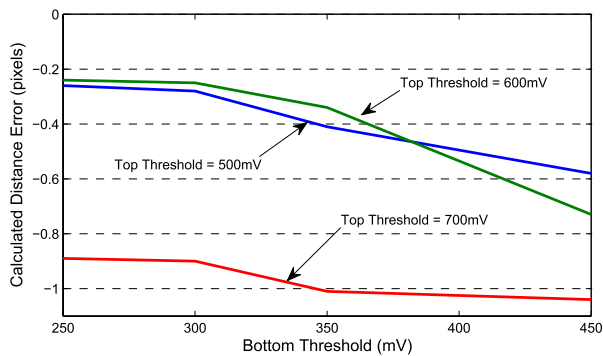


Fig. 15. Calculated distance error with different top threshold voltage.

factors including non-ideality of optics, sensor and readout circuit noise and ADC noise. The reduced magnitude of the pixel response, that is the reduced voltage difference between the reset voltage and readout voltage, causes a degraded SNR. Moreover, the missing readouts inside the “star” object can also affect the centroiding error to increase. As is in the case in Fig. 12(d), the absolute calculated error is increased to 0.58 pixels. This is primarily due to the centroiding method that calculates the weighted center of a mass of pixels. If there are missing readouts inside the pixel mass, the calculated center will be shifted, resulting in the increase of distance calculation error.

### B. Discussion

The two threshold voltages that form the readout window are critical parameters. According to our simulation and measurement results, the readout window is supposed to be as large as possible to reduce the possibility for a pixel to fall out of the range. As for the bottom threshold, it should be kept as low as possible to expand the readout window. Normally, it should be kept at a value slightly higher than the saturation level so that the “marked-off” pixels will not trigger the readout twice falsely. In this design, the bottom threshold can be set as low as 180mV, which is slightly above the saturation voltage of the pixel (150mV after the source follower according to the simulation results). This voltage slack is big enough to avoid false detection. Top threshold, on one hand, should be high enough to guarantee a large readout window to initiate readout of “bright” pixels quickly after the exposure so as to reduce readout congestion for the rest of the pixels. On the other hand, top threshold also restricts the minimal signal magnitude, which has a critical effect on the SNR. The higher the top threshold, the easier it is for the pixels to fall into the readout window. Pixels are likely to have small signal magnitudes when they are sampled. This results in degraded SNR for those pixels. The test results shows that the “stars” can be barely captured when the top threshold is above 700mV, which appears falsely merged with the dark background. For all “star” images taken with 10klux light source, the top threshold is supposed to be set near or below half of the signal swing so that the “stars” can receive enough photons before readout to maintain acceptable SNR.

There is possibility that pixel voltage falls out of the readout window between two rounds of scanning. This can happen

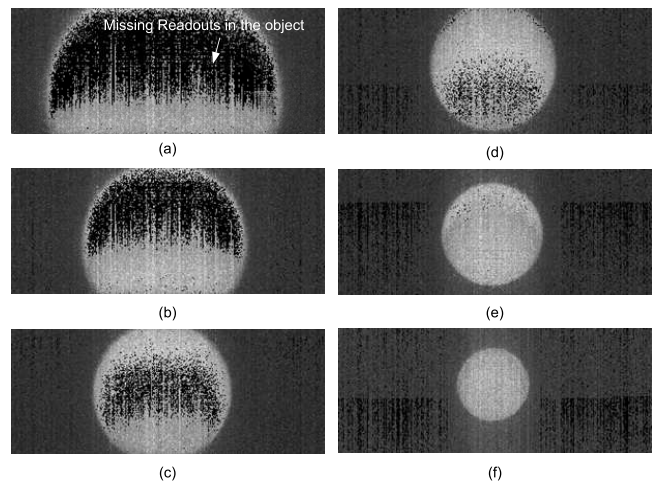


Fig. 16. Example images of uniform circular objects with different size.

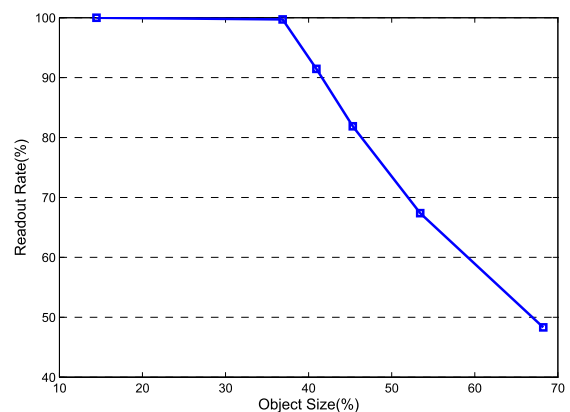


Fig. 17. Readout percentage for the pixels inside the objects.

when a large block of pixels have similar intensity and thus takes longer time to finish the scan. Therefore higher readout speed or more readout channels should be used for a higher resolution imager. Fig. 16 shows captured images of uniform-intensity circles with different size under aforementioned readout window size and Fig. 17 shows the readout percentage for the pixels inside the objects, respectively. When the circle is small, similar to the size of the “star” objects, the readout is able to handle all the readout requests in time. When the size of the object increases, black pixels inside the object appear since these pixel are missing during the readout and hence are regarded as dark pixels. It is worthy to note that the worst case happens if the entire pixel array is projected by a uniform intensity. The long waiting time may cause other pixels to saturate, or in other words, to fall out of the readout window.

## VI. CONCLUSION

In this paper, we have introduced a novel CMOS image sensor architecture for star tracker application that allows adaptive integration time. Brighter pixels will be detected and read out at an earlier time to avoid saturation and dimmer pixels can have longer integration time. Due to the voltage detection nature of the sensor architecture, it can be categorized into the saturation detection scheme. Compared with other solutions in this category, the pixel maintains compact footprint and high

fill factor. The shrinking size of the pixels can be beneficial to high-resolution integration to increase the field of view in star tracker. A proof-of-concept chip has been fabricated in Global Foundries 0.18 $\mu\text{m}$  1P6M CMOS technology. According to our simulation and experimental results, the architecture demonstrates a great potential for star tracker applications where pixel intensities are sparsely distributed. Due to the use of readout window and cyclical scanning, a pixel has the chance to fall out of the readout window between two consecutive rounds of scanning. The possibility of the missing readout is related to readout bandwidth and pixel intensity distribution across the pixel array. Higher readout speed or more readout channels should be adopted for high resolution integration.

## REFERENCES

- [1] M. Pham, K.-S. Low, and S. Chen, "An autonomous star recognition algorithm with optimized database," *IEEE Trans. Aerosp. Electron. Syst.*, vol. 49, no. 3, pp. 1467–1475, Jul. 2013.
- [2] C. Liebe, "Accuracy performance of star trackers—A tutorial," *IEEE Trans. Aerosp. Electron. Syst.*, vol. 38, no. 2, pp. 587–599, Apr. 2002.
- [3] A. Spivak, A. Belenky, A. Fish, and O. Yadid-Pecht, "Wide-dynamic-range CMOS image sensors: Comparative performance analysis," *IEEE Trans. Electron Devices*, vol. 56, no. 11, pp. 2446–2461, Nov. 2009.
- [4] G. Storm, R. Henderson, J. Hurwitz, D. Renshaw, K. Findlater, and M. Purcell, "Extended dynamic range from a combined linear-logarithmic CMOS image sensor," *IEEE J. Solid-State Circuits*, vol. 41, no. 9, pp. 2095–2106, Sep. 2006.
- [5] K. Hara, H. Kubo, M. Kimura, F. Murao, and S. Komori, "A linear-logarithmic CMOS sensor with offset calibration using an injected charge signal," in *IEEE ISSCC Dig. Tech. Papers*, vol. 1, Feb. 2005, pp. 354–603.
- [6] M. Vatteroni, P. Valdastrì, A. Sartori, A. Menciassi, and P. Dario, "Linear-logarithmic CMOS pixel with tunable dynamic range," *IEEE Trans. Electron Devices*, vol. 58, no. 4, pp. 1108–1115, Apr. 2011.
- [7] N. Akahane, S. Sugawa, S. Adachi, K. Mori, T. Ishiuchi, and K. Mizobuchi, "A sensitivity and linearity improvement of a 100-dB dynamic range CMOS image sensor using a lateral overflow integration capacitor," *IEEE J. Solid-State Circuits*, vol. 41, no. 4, pp. 851–858, Apr. 2006.
- [8] N. Ide, W. Lee, N. Akahane, and S. Sugawa, "A wide DR and linear response CMOS image sensor with three photocurrent integrations in photodiodes, lateral overflow capacitors, and column capacitors," *IEEE J. Solid-State Circuits*, vol. 43, no. 7, pp. 1577–1587, Jul. 2008.
- [9] N. Akahane, R. Ryuzaki, S. Adachi, K. Mizobuchi, and S. Sugawa, "A 200-dB dynamic range iris-less CMOS image sensor with lateral overflow integration capacitor using hybrid voltage and current readout operation," in *IEEE ISSCC Dig. Tech. Papers*, Feb. 2006, pp. 1161–1170.
- [10] M. Mase, S. Kawahito, M. Sasaki, Y. Wakamori, and M. Furuta, "A wide dynamic range CMOS image sensor with multiple exposure-time signal outputs and 12-bit column-parallel cyclic A/D converters," *IEEE J. Solid-State Circuits*, vol. 40, no. 12, pp. 2787–2795, Dec. 2005.
- [11] J. Lee, I. Baek, and K. Yang, "Memoryless wide-dynamic-range CMOS image sensor using nonfully depleted PPD-storage dual capture," *IEEE Trans. Circuits Syst. II, Exp. Briefs*, vol. 60, no. 1, pp. 26–30, Jan. 2013.
- [12] D. Stoppa, M. Vatteroni, D. Covi, A. Baschiroto, A. Sartori, and A. Simoni, "A 120-dB dynamic range CMOS image sensor with programmable power responsivity," *IEEE J. Solid-State Circuits*, vol. 42, no. 7, pp. 1555–1563, Jul. 2007.
- [13] D. Stoppa, A. Simoni, L. Gonzo, M. Gottardi, and G.-F. Dalla Betta, "Novel CMOS image sensor with a 132-dB dynamic range," *IEEE J. Solid-State Circuits*, vol. 37, no. 12, pp. 1846–1852, Dec. 2002.
- [14] C. Posch, D. Matolin, and R. Wohlgenannt, "A QVGA 143-dB dynamic range frame-free PWM image sensor with lossless pixel-level video compression and time-domain CDS," *IEEE J. Solid-State Circuits*, vol. 46, no. 1, pp. 259–275, Jan. 2011.
- [15] S. Chen, A. Bermak, and Y. Wang, "A CMOS image sensor with on-chip image compression based on predictive boundary adaptation and memoryless QTD algorithm," *IEEE Trans. Very Large Scale Integr. (VLSI) Syst.*, vol. 19, no. 4, pp. 538–547, Apr. 2011.
- [16] C. Shoushun, F. Boussaid, and A. Bermak, "Robust intermediate readout for deep submicron technology CMOS image sensors," *IEEE Sensors J.*, vol. 8, no. 3, pp. 286–294, Mar. 2008.
- [17] H. Fiedler, B. Hoefflinger, W. Demmer, and P. Draheim, "A 5-bit building block for 20 MHz A/D converters," *IEEE J. Solid-State Circuits*, vol. 16, no. 3, pp. 151–155, Jun. 1981.
- [18] P. Figueiredo and J. Vital, "Low kickback noise techniques for CMOS latched comparators," in *Proc. ISCAS*, vol. 1, May 2004, pp. 537–540.



**Xinyuan Qian** received the B.S. degree in electrical engineering from Shanghai Jiao Tong University, Shanghai, China, in 2006, and the M.S. degree in electrical engineering from the Technical University of Munich, Munich, Germany, in 2008. He is currently pursuing the Ph.D. degree at the School of Electrical and Electronic Engineering, Nanyang Technological University, Singapore.

His current research interests include high dynamic range CMOS image sensors and smart vision sensors for space applications.



**Hang Yu** received the B.S. degree in microelectronics from Peking University, Beijing, China, in 2007, and the M.E. degree in computer science from the Institute of Computing Technology, Chinese Academy of Sciences, Beijing, in 2010. He joined Nanyang Technological University, Singapore, as a Research Associate, in 2010.

His current research interests include smart vision sensors, time-delay-integration image sensors, and motion detection sensors.



**Shoushun Chen** (M'05) received the B.S. degree from Peking University, Beijing, China, the M.E. degree from the Chinese Academy of Sciences, Beijing, and the Ph.D. degree from the Hong Kong University of Science and Technology, Hong Kong, in 2000, 2003, and 2007, respectively.

He held a post-doctoral research fellowship with the Department of Electronic and Computer Engineering, Hong Kong University of Science and Technology. From February 2008 to May 2009, he was a Post-Doctoral Research Associate within the

Department of Electrical Engineering, Yale University, New Haven, CT, USA. In July 2009, he joined Nanyang Technological University, Singapore, as an Assistant Professor.

Dr. Chen serves as a Technical Committee Member of Sensory Systems, the IEEE Circuits and Systems Society, an Associate Editor of the IEEE SENSORS JOURNAL, a Program Director (Smart Sensors) of VIRTUS, IC Design Centre of Excellence, NTU. His current research interests include smart vision sensors, motion detection sensors, energy-efficient algorithms for bio-inspired vision, and analog/mixed-signal VLSI circuits and systems.



**Kay-Soon Low** (M'88–SM'00) received the B.Eng. degree in electrical engineering from the National University of Singapore, Singapore, and the Ph.D. degree in electrical engineering from the University of New South Wales, Sydney, Australia.

He joined the School of Electrical and Electronic Engineering, Nanyang Technological University, Singapore, in 1994, as a Lecturer, and subsequently became an Associate Professor. He has served as a consultant to many companies and has a number of granted patents on nonlinear

circuits and UWB systems. His funded projects are in the field of wearable wireless sensor network, solar energy system, pulse neural network, and satellite system. He has been the Centre Director of Satellite Research Centre, Nanyang Technological University since 2009.